Available online at www.sciencedirect.com

SciVerse ScienceDirect

Ceramics International 38 (2012) 4797–4811

CERAMICS INTERNATIONAL

www.elsevier.com/locate/ceramint

Experimental investigation and mathematical modeling of oxygen permeation through dense $Ba_{0.5}Sr_{0.5}Co_{0.8}Fe_{0.2}O_{3-\delta}$ (BSCF) perovskite-type ceramic membranes

Amir Behrouzifar [a], Amir Atabak Asadi [a], Toraj Mohammadi [a,*], Afshin Pak [b]

[a] *Research Centre for Membrane Separation Processes, Chemical Engineering Department, Iran University of Science and Technology (IUST), Narmak, Tehran, Iran*

[b] *Engineering Department of Oil & Gas Special Projects, Iranian Central Oil Field Company, Tehran, Iran*

Received 5 February 2012; received in revised form 20 February 2012; accepted 21 February 2012
Available online 3 March 2012

Abstract

$Ba_{0.5}Sr_{0.5}Co_{0.8}Fe_{0.2}O_{3-\delta}$ (BSCF) perovskite powder was synthesized via EDTA/citrate complexation method. BSCF membranes were formed by pressing powder at 400 MPa and sintering at 1100 °C for 10 h. XRD patterns showed that a high pure powder with cubic structure was obtained. SEM micrographs revealed that the membranes are dense with large grains. Effects of temperature, feed and permeate side oxygen partial pressures, flow rates and membrane thickness on oxygen permeation flux were studied experimentally. A Nernst–Planck based mathematical model, including surface exchange kinetics and bulk diffusion, was developed to predict oxygen permeation flux. Considering non-elementary surface reactions and introducing system hydrodynamics into the model resulted in an excellent agreement (RMSD = 0.0617, AAD = 0.0487 and R^2 = 0.985) between predicted and measured fluxes. The results showed that oxygen permeation flux increases with temperature, feed side oxygen partial pressure and flow rates, however decreases with permeate side oxygen partial pressure and membrane thickness. Contribution of feed side surface exchange reactions, bulk diffusion and permeate side surface exchange reactions resistances in the total resistance are in the range of 8–32%, 10–81% and 11–59%, respectively. Permeation rate-limiting step was determined using the membrane dimensionless characteristic thickness.

Keywords: C. Diffusion; D. Perovskite; E. Membranes; Mathematical modeling

1. Introduction

Oxygen has many usages in different industries including metal production, chemicals, petroleum refining, coal gasification, etc. [1]. In many of these applications, air is used as oxygen source, but in some industries enriched air or pure oxygen is needed [2]. Mixed-conducting dense ceramic membranes have the potential to produce ultrapure oxygen at large volumes, low costs and high efficiencies [1]. Many types of ceramic materials can be used as dense membranes for air separation. Among them, perovskite type materials have been attracted more attention because of their higher oxygen flux and excellent stability [3].

$SrCoO_{3-\delta}$ is a significant perovskite-type parent material. Among different phase structures of $SrCoO_{3-\delta}$, the oxide with a cubic structure has the highest conductivity [4]. Substitution of either the A- or B-site has been widely applied to stabilize the cubic lattice structure of $SrCoO_{3-\delta}$ [5–7]. Structural stability and oxygen permeation flux of $Ba_{0.5}Sr_{0.5}Co_{0.8}Fe_{0.2}O_{3-\delta}$ (BSCF) developed by Shao et al. [8] were remarkably enhanced compared with $SrCoO_{3-\delta}$ and its other derivatives. Thereafter, oxygen permeability [9–11], conductivity [12], stability [13] and mechanical properties [14,15] of BSCF have been studied by several research groups. However, the oxygen permeation flux of BSCF membranes decreases with time in long-term experiments [16]. Because Co is also expensive, it may not be the perfect material for practical applications [16].

Oxygen permeation flux through perovskite membranes is a function of many parameters. The most important is the membrane composition, e.g. the $BaCoO_3$ and $SrCoO_3$

* Corresponding author. Tel.: +98 21 77240496; fax: +98 21 77240495.
E-mail address: torajmohammadi@iust.ac.ir (T. Mohammadi).

0272-8842/$36.00
doi:10.1016/j.ceramint.2012.02.068

perovskites exhibit high oxygen conduction, but the $BaCeO_3$ and $SrCeO_3$ are not oxygen permeable perovskites and actually are proton conductors [3]. Preparation methods also affect membranes permeability. Temperature, membrane thickness, upstream oxygen concentration, feed and permeate side pressures, feed and sweep gas flow rates, feed impurities even at very low concentrations and membrane age also affect oxygen permeation flux of the membranes. Experimental study of these factors is time and money consuming, so an accurate and simple model can be very useful. Many researchers attempted to model oxygen permeation flux through perovskite membranes [17–23]. These models were somehow successful in studying oxygen permeation flux through perovskite-type membranes. However, in all of these models, surface reactions of oxygen oxidation and reduction were considered elementary, and in most of them effects of flow rates were ignored.

In this paper, effects of temperature, membrane thickness, feed and permeate side oxygen partial pressures and feed and sweep gas flow rates on oxygen permeation flux through the $Ba_{0.5}Sr_{0.5}Co_{0.8}Fe_{0.2}O_{3-\delta}$ membranes were studied. A mathematical model, which relates oxygen permeation flux to all operating parameters, was also developed. With the aid of improvements which were made, accuracy of the model predictions was significantly enhanced. Moreover, oxygen vacancy diffusion coefficient and activation energy of surface reactions, and also contribution of different resistances to oxygen permeation flux, and finally dimensionless characteristic thickness of the membranes were calculated.

2. Experimental

2.1. Membrane preparation

Due to advantages such as carbonate-free and chemically homogeneous final oxide powder with a high relative density [24], the BSCF powder was synthesized using the EDTA/citrate complexation method [8]. Metallic nitrates ($Ba(NO_3)_2$, $Sr(NO_3)_2$, $Co(NO_3)_2{\cdot}6H_2O$, and $Fe(NO_3)_3{\cdot}9H_2O$), EDTA acid ($C_{10}H_{16}N_2O_8$), citric acid ($C_6H_8O_7$), and ammonia solution ($NH_3{\cdot}H_2O$ 25 wt.%), all purchased from Merck Co with analytical grade, were used in this method. Initially calculated amount of EDTA acid was added to ammonia solution and was dissolved under heating and stirring. After that, by heating and stirring, a required amount of $Ba(NO_3)_2$ was dissolved into this solution. Then, in another beaker, required amounts of $Sr(NO_3)_2$, $Co(NO_3)_2{\cdot}6H_2O$, and $Fe(NO_3)_3{\cdot}9H_2O$ were dissolved in deionized water. Next, the later solution was added to the former solution. Then, citric acid was dissolved in the final solution by heating and stirring. The mole ratio of EDTA acid:citric acid:total metal ions was controlled to be around 1:1.5:1. By addition of $NH_3{\cdot}H_2O$, pH value of the final solution was fixed around 6. A calibrated digital pH meter (EcoMet P25, istek, Inc.) was used to control the pH within ±0.01 of the set point. By evaporation of water under heating and stirring, a dark purple gel was obtained after several hours. The formed gel was dried overnight in an oven (Memmert GmbH + Co.KG) at 150 °C and finally a black porous compound was obtained. The primary powder was obtained after grinding the porous compound. Then, to obtain the final BSCF powder, the primary powder was calcined in an electric furnace (EX1200-30L, Exciton) at 950 °C for 5 h with heating and cooling rate of 1 °C/min. Temperature of the furnace was controlled with a PID controller (PX9, Hanyoung) within ±1 °C of the set point. The BSCF powder was ground and pressed into disk in a stainless steel mould (17.5 mm i.d.) under a hydraulic pressure of 400 MPa. The green disk was sintered in the electric furnace at 1100 °C for 10 h with heating and cooling rates of 1 °C/min. The densities of the sintered membranes were determined by the Archimedes method. Only those membranes that had relative densities higher than 90% were used for oxygen permeation studies.

2.2. Membrane characterization

Phase structure of the as-synthesized BSCF powder was characterized at room temperature by X-ray diffraction (XRD, PW3710, Philips) with Cu Kα radiation and Ni filter in the 2θ range of 4–90° with scan rate of 1°/min and 0.02° intervals. Morphology and microstructure of surface and cross section of the sintered BSCF membrane and the BSCF powder were also examined by scanning electron microscopy (VEGA II SBU, TESCAN). Densities of the BSCF powders were measured using a gas pycnometer (AccuPyc 1330, Micrometrics, USA). Relative densities of the sintered membranes was defined as $(\rho/\rho_0) \times 100\%$, where ρ_0 was the powder density measured by the gas pycnometer, and ρ was the actual density measured by the Archimedes method.

2.3. Oxygen permeation

Oxygen permeation flux through the BSCF membrane was measured using a permeation apparatus, as shown in Fig. 1. The disk-shaped BSCF membrane was placed in a heat resistant stainless steel permeation module as shown in Fig. 2. To seal the module, a high temperature ceramic binder (Fire Sealant

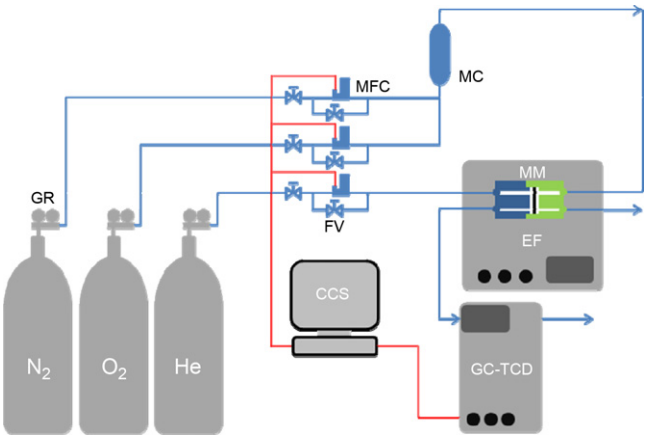

Fig. 1. Apparatus used for oxygen permeation measurement (GR, gas regulator; FV, flow valve; MC, mixing chamber; MFC, mass flow controller; MM, membrane module; EF, electric furnace; GC, gas chromatography; TCD, thermal conductivity detector; CCS, computerized control system).

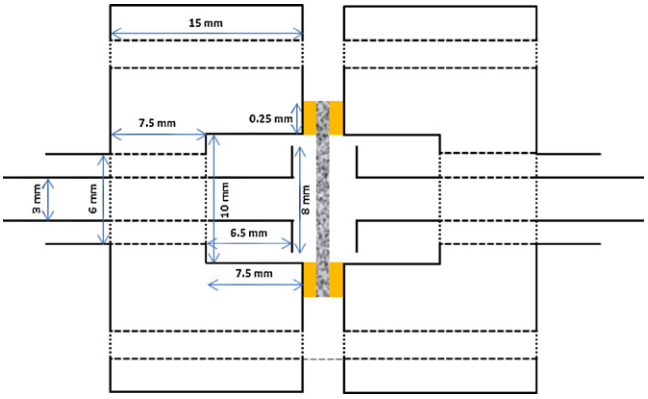

Fig. 2. Membrane module.

1200 °C, Den Braven Sealants BV, Netherlands) was used at both sides of the membrane. Sealing was performed at room temperature. After raising temperature to working temperature, initially a nitrogen leakage test was performed to ensure gas tightness and then oxygen permeation was carried out. The effective membrane diameter for oxygen permeation was 1.0 cm. The membrane module was mounted in an electric furnace. Flow rates of the inlet gases were controlled by mass flow controllers (5850E Series, 5050E/B1A1B20, BROOKS, Instrument BV). Synthetic air or $O_2 + N_2$ mixtures were introduced into the membrane upstream side. High purity helium, as sweep gas for the permeating oxygen, was fed to the membrane downstream side. Both upstream and downstream sides were maintained at atmospheric pressure. Effects of temperature, feed side oxygen partial pressure, feed and sweep gas flow rates and membrane thickness were investigated on oxygen permeation flux. As shown in Table 1, 7 levels of temperature and 5 levels of other parameters were used in this study. Synthetic air was used in all the experiments except for those in which the feed side oxygen partial pressure was studied. Also, to study effect of the feed side oxygen partial pressure, feed flow rate of 300 cm^3/min was used. The permeate stream was analyzed by a calibrated gas chromatography instrument (GC-2001M, Sanayeh Teif Gostar Co., Iran) which was equipped with a thermal conductivity detector (TCD) and a 2 m 5 Å molecular sieves with argon as carrier gas.

The amount of nitrogen leakage was negligible in almost all the experiments and in most cases no nitrogen leakage was detected. It is reasonable to assume that the nitrogen and oxygen leakage through pores or cracks is in accordance with the Knudsen diffusion mechanism. So the permeation flux through the perovskite structure was calculated as follows:

$$J_{O_2} = \left[C^P_{O_2} - C^P_{N_2} \times \frac{0.21}{0.79} \times \left(\frac{28}{32}\right)^{1/2} \right] \times \frac{F}{S} \quad (1)$$

where J_{O_2} is oxygen permeation flux in $cm^3/(cm^2\ min)$, $C^P_{O_2}$ and $C^P_{N_2}$ are measured concentrations of oxygen and nitrogen in the permeate side stream, respectively, F is flow rate of the gas on the permeate side in cm^3/min, and S is the membrane surface area (0.785 cm^2). The permeation calculation was performed based on the outlet gas flow rate instead of the inlet He flow rate to prevent any error related to the He leakage.

3. Model development

3.1. Introductory model

The Wagner equation is mostly accepted for predicting oxygen permeation flux through perovskite membranes [25]. However in this equation, only effect of bulk diffusion is considered and surface-exchange reactions are neglected. For thick and thin membranes, bulk diffusion and surface-exchange reactions are more important, respectively. However, the Nernst–Planck based models consider both bulk diffusion and surface-exchange reactions. In fact, the Wagner equation is a simplified case of the Nernst–Planck equation. The Nernst–Planck equation describes flux of charged species in any ionic solution and especially in a mixed conductor in which oxygen ion, oxygen vacancy, proton, electron and electron hole are charged species [26]:

$$\vec{J}_i = -\frac{\sigma_i}{z_i^2 F^2} \vec{\nabla} \tilde{\mu}_i + C_i \vec{v} \quad (2)$$

In derivation of the Nernst–Planck equation, linear approximation is used (i.e. $\vec{J}_i = -\sum_k l_{i,k} \vec{\nabla} \tilde{\mu}_k + C_i \vec{v}$) and cross-phenomenological coefficients are neglected (i.e. $l_{i,k} = 0$ if $i \neq k$). With applying the two following assumptions to the Nernst–Planck equation, Eq. (3) can be derived [26]:

(1) deviations from the Nernst–Einstein equation (i.e. $\sigma_i = (z_i^2 F^2 / \bar{R}T) C_i D_i$) due to for example electrophoretic contributions are negligible;
(2) gradient of activity coefficient is negligible (i.e. activity coefficient is independent of concentration)

$$\vec{J}_i = -D_i \left(\vec{\nabla} C_i + \frac{z_i F}{\bar{R}T} C_i \vec{\nabla} \phi \right) + C_i \vec{v} \quad (3)$$

Table 1
The experimental parameters and their levels for oxygen permeation measurements.

Parameter	Levels	Dimension
Temperature	650, 700, 750, 800, 850, 900, and 950	°C
Feed side oxygen partial pressure	0.1, 0.3, 0.5, 0.7 and 0.9	atm
Feed flow rate	25, 50, 100, 150 and 200	cm^3/min
Sweep gas flow rate	20, 40, 60, 80 and 100	cm^3/min
Membrane thickness	0.25, 0.5, 0.75, 1.0 and 1.5	mm

In mixed ionic-electronic conducting ceramics, electronic species flow through the membrane and consequently no external current is imposed. Also, local velocity of the inert marker is negligible. With these assumptions, the following equation can be derived [27]:

$$\vec{J}_i = -D_i C_i \left[\frac{1-t_i}{C_i} \vec{\nabla} C_i - \sum_{j \neq i} \frac{z_i}{z_j} \frac{t_j}{C_j} \vec{\nabla} C_j \right] \tag{4}$$

However, Eq. (4) is still very complicated to be used and some assumptions, based on system characteristic, are needed. With the following six assumptions, Eq. (5) can be derived for oxygen permeation through ion-conducting membranes with a high ratio of electronic to ionic conductivity like perovskites [19]:

(1) one-dimensional model is applied;
(2) oxygen vacancy and electron hole are the only mobile charges;
(3) electronic conductivity is much greater than ionic conductivity in perovskites, i.e. ionic transference number approaches to zero, so oxygen permeation rate across the membrane is governed by flux of oxygen vacancies;
(4) electron hole concentrations are essentially constant on the both membrane surfaces and the law of mass action is applied for other components;
(5) surface reactions on the both membrane surfaces are elementary and the forward reaction on one side of the membrane is equal to the reverse reaction on the other side;
(6) diffusion coefficient of oxygen vacancies does not vary with position and is only a function of temperature.

$$J_{O_2} = \frac{(k_r/k_f)[(1/p''^{0.5}_{O_2}) - (1/p'^{0.5}_{O_2})]}{[1/(k_f p'^{0.5}_{O_2})] + [2L/D_V] + [1/(k_f p''^{0.5}_{O_2})]} \tag{5}$$

Oxygen vacancy diffusion coefficient and both forward and reverse reaction rate constants are strong functions of temperature. Usually the Arrhenius type equation is used to describe temperature dependence of these parameters:

$$D_V = D_V^0 \exp\left(-\frac{E_D}{\bar{R}T}\right) \tag{6a}$$

$$k_f = k_f^0 \exp\left(-\frac{E_f}{\bar{R}T}\right) \tag{6b}$$

$$k_r = k_r^0 \exp\left(-\frac{E_r}{\bar{R}T}\right) \tag{6c}$$

However, by applying Eq. (5) to predict experimental oxygen permeation data, it is concluded that this equation cannot estimate oxygen permeation flux accurately. To improve its precision, three correction terms can be introduced into the equation: one takes into account deviation from elementary reactions and the two others considering effects of feed and sweep gas flow rates.

3.2. Effects of non-elementary surface reactions

The following reversible reactions take place on the membrane surface at feed and permeate sides, respectively:

$$\frac{1}{2}O_2 + V_O^{\bullet\bullet} \overset{k_f/k_r}{\longleftrightarrow} O_O^{\times} + 2h^{\bullet} \tag{7a}$$

$$O_O^{\times} + 2h^{\bullet} \overset{k_r/k_f}{\longleftrightarrow} \frac{1}{2}O_2 + V_O^{\bullet\bullet} \tag{7b}$$

In derivation of Eq. (5), it is assumed that these reactions are elementary with the following reaction rates [19]:

$$J_{O_2} = k_f p'^{0.5}_{O_2} C'_V - k_r \tag{8a}$$

$$J_{O_2} = k_r - k_f p''^{0.5}_{O_2} C''_V \tag{8b}$$

However, these reactions are not necessarily elementary [28] and involve many sub-steps, such as oxygen adsorption, dissociation, charge transfer, bulk diffusion, recombination and desorption [29]. Overall oxygen transport rate may be limited by any of these sequential steps:

$$\frac{1}{2}O_{2\langle g'\rangle} \leftrightarrow \frac{1}{2}O_{2\langle s'\rangle} \tag{9a}$$

$$\frac{1}{2}O_{2\langle s'\rangle} \leftrightarrow O_{\langle s'\rangle} \tag{9b}$$

$$O_{\langle s'\rangle} + V_{O\langle s'\rangle}^{\bullet\bullet} \leftrightarrow O_{O\langle s'\rangle}^{\times} + 2h_{\langle s'\rangle}^{\bullet} \tag{9c}$$

$$O_{O\langle s'\rangle}^{\times} \leftrightarrow O_{O\langle s''\rangle}^{\times} \tag{9d}$$

$$h_{\langle s'\rangle}^{\bullet} \leftrightarrow h_{\langle s''\rangle}^{\bullet} \tag{9e}$$

$$O_{O\langle s''\rangle}^{\times} + 2h_{\langle s''\rangle}^{\bullet} \leftrightarrow O_{\langle s''\rangle} + V_{O\langle s''\rangle}^{\bullet\bullet} \tag{9f}$$

$$O_{\langle s''\rangle} \leftrightarrow \frac{1}{2}O_{2\langle s''\rangle} \tag{9g}$$

$$\frac{1}{2}O_{2\langle s''\rangle} \leftrightarrow \frac{1}{2}O_{2\langle g''\rangle} \tag{9h}$$

As mentioned before, it is reasonable to consider electron hole concentration constant at the both membrane surfaces, thus the reverse reaction rate of Eq. (7a) and the forward reaction rate of Eq. (7b) are zero-order. On the other hand, it is fair to consider a non-elementary reaction order respect to oxygen partial pressure and oxygen vacancy concentration. Therefore, Eqs. (8a) and (8b) can be rewritten in the following forms:

$$J_{O_2} = k_f p'^{n}_{O_2} C'^{m}_V - k_r \tag{10a}$$

$$J_{O_2} = k_r - k_f p''^{n}_{O_2} C''^{m}_V \tag{10b}$$

However, considering non-elementary reaction order for oxygen vacancy, leads to an implicit equation for oxygen permeation flux, which is not suitable. Thus, considering an elementary order for oxygen vacancy concentration and a non-elementary order for oxygen partial pressure, leads to the following equations for feed and permeate sides of the

membrane, respectively:

$$J_{O_2} = k_f p'^{n}_{O_2} C'_V - k_r \quad (11a)$$

$$J_{O_2} = k_r - k_f p''^{n}_{O_2} C''_V \quad (11b)$$

Combining Eqs. (11a) and (11b) with Eq. (4) and using assumptions stated above result in Eq. (12) to calculate oxygen permeation flux:

$$J_{O_2} = \frac{(k_r/k_f)[(1/p''^{n}_{O_2}) - (1/p'^{n}_{O_2})]}{[1/(k_f p'^{n}_{O_2})] + [2L/D_V] + [1/(k_f p''^{n}_{O_2})]} \quad (12)$$

3.3. Effects of feed and sweep gas flow rates

Using Eq. (12) for predicting oxygen permeation flux through the BSCF membranes showed superior improvements in accuracy. However, there is still a gap between the experimental data and the model predictions. Experiments showed that feed and sweep gas flow rates have considerable effect on oxygen permeation flux. However, in Eq. (12), there is no term to reflect theses effects. To derive a much more accurate model, the effect of feed and sweep gas flow rates should be taken into account. Modified oxygen partial pressure, which takes the flow rate into account, can be defined for each side of the membrane. It is clear that oxygen partial pressure at each side of the membrane is affected by the gas flow rate. Thus, a modified oxygen partial pressure, consisting of the oxygen partial pressure and a correction term containing a Reynolds number (Re) can be introduced [28]. After examining several different functionalities of Re number, finally the following equations were proposed for the feed and permeate sides modified oxygen partial pressures, respectively:

$$p'^{*}_{O_2} = (a' + b' \mathrm{R}e'^{c'}) p'_{O_2} \quad (13a)$$

$$p''^{*}_{O_2} = (a'' + b'' \mathrm{R}e''^{c''}) p''_{O_2} \quad (13b)$$

Re numbers are defined in the following way:

$$\mathrm{R}e' = q'/(\pi \nu' \lambda') \quad (14a)$$

$$\mathrm{R}e'' = q''/\pi \nu'' \lambda'' \quad (14b)$$

Substitution of these modified oxygen partial pressures in Eq. (12) results in Eq. (15). The results showed that implementation of the above three correction terms for calculation of oxygen permeation flux through the BSCF membranes results in excellent agreement between the model predictions and the experimental data.

$$J_{O_2} = \frac{(k_r/k_f)[(1/p''^{*n}_{O_2}) - (1/p'^{*n}_{O_2})]}{[1/(k_f p'^{*n}_{O_2})] + [2L/D_V] + [1/(k_f p''^{*n}_{O_2})]} \quad (15)$$

3.4. Contribution of resistances

Three main different resistances contribute to total resistance of oxygen permeation: resistances of surface exchange kinetics on both sides of the membrane and bulk diffusion resistance. As known, flux is ratio of driving force to resistance. From Eq. (15), it is obvious that numerator is the driving force and denominator is the resistance. As seen, the denominator is sum of surface exchange resistance on feed side, bulk diffusion resistance, and surface exchange resistance on permeate side, respectively. These resistances are summarized in Table 2. Using definition of resistances and Eq. (15), it can be concluded that if any step has limiting rate, its resistance dominates total resistance, so oxygen permeation flux across the membrane is mainly affected by that resistance. Oxygen permeation fluxes for each limiting case are summarized in the last column of Table 2.

3.5. Dimensionless characteristic thickness

As known, oxygen permeation flux increases by reducing membrane thickness, until the thickness becomes less than a characteristic value (L_c). For a membrane with its characteristic thickness, oxygen permeation flux is controlled by both surface exchange kinetics and bulk diffusion. In the other hand, for the thinner membranes than the characteristic thickness, oxygen permeation flux can only marginally be improved by making the membrane thinner. To investigate the effect of membrane thickness, the characteristic thickness of the BSCF membranes can be defined as follows [30]:

$$L_c = D_V/k_s \quad (16)$$

In this relation, k_s is the average surface exchange coefficient and given by:

$$\frac{1}{k_s} = \frac{1}{2}(R'_{ex} + R''_{ex}) \quad (17)$$

Table 2
Resistances and oxygen permeation flux at different limiting conditions.

Limiting case	Resistance	Oxygen permeation flux
Surface exchange on the feed side	$R'_{ex} = 1/(k_f p'^{*n}_{O_2})$	$J_{O_2} = k_r[(p'^{*}_{O_2}/p''^{*}_{O_2})^n - 1]$
Bulk diffusion	$R_{diff=\frac{2L}{D_V}}$	$J_{O_2} = \frac{(k_r/k_f)[(1/p''^{*n}_{O_2}) - (1/p'^{*n}_{O_2})]}{2L/D_V}$
Surface exchange on the permeate side	$R''_{ex} = 1/(k_f p''^{*n}_{O_2})$	$J_{O_2} = k_r[1 - (p''^{*}_{O_2}/p'^{*}_{O_2})^n]$

Combination of equations presented in the second column of Table 2 with Eqs. (16) and (17) results in the following equation for the membrane characteristic thickness:

$$L_c = \frac{D_V}{2k_f}\left(\frac{1}{p_{O_2}^{\prime *n}} + \frac{1}{p_{O_2}^{\prime\prime *n}}\right) \tag{18}$$

To more easily determine the mechanism which controls oxygen permeation flux, it is reasonable to define the membrane dimensionless characteristic thickness (L_{cr})

$$L_{cr} = \frac{L}{L_c} = \frac{R_{diff}}{R'_{ex} + R''_{ex}} \tag{19}$$

If the value of L_{cr} is greater than unity, bulk diffusion mechanism is the rate-limiting step of oxygen transport process. Otherwise, surface exchange reactions control oxygen permeation.

4. Results and discussion

4.1. Characterization

The room temperature X-ray diffraction pattern of the synthesized BSCF powder is shown in Fig. 3. The XRD pattern shows seven strong diffraction peaks. It was well indexed as a cubic perovskite structure with the lattice parameter $a = 0.39791$ nm and space group of Pm3m (2 2 1). Formation of cubic perovskite structure reveals that large part of the B-site cations in the BSCF are in the form of lower oxidation state indicating that the tolerance factor for the BSCF perovskite is around 1. Koster and Mertins [31] reported XRD data for BSCF. The corresponding Rietveld refined unit cell parameter is 0.39830 nm at room temperature which is very close to the value obtained in this work. The average crystallite size of the powders, calculated by the Scherrer formula from the XRD data, is around 40.6 nm.

SEM micrographs of the membrane surface and cross section are shown in Fig. 4. As these micrographs reveal, the membrane surface is completely dense and crack free. Although some pores appeared on the cross section of sintered membranes, they were verified to be closed pores by gas tightness testing using nitrogen. Also, these pores were very small compared with the membrane thickness and their average diameter was less than 1% of the membrane thickness.

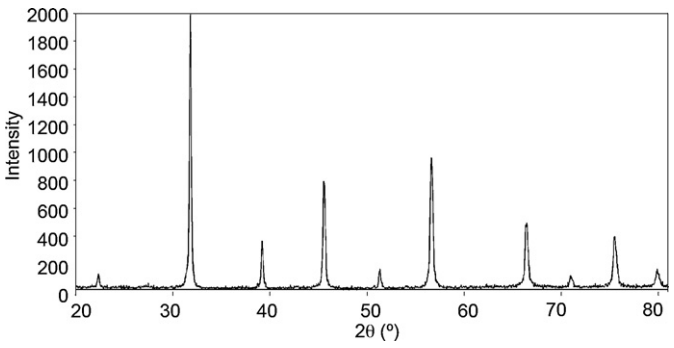

Fig. 3. XRD pattern of the BSCF powder.

Analyzing the SEM images at lower magnification showed that the grain size is within the range 10–100 μm. The relative densities of the BSCF membranes are in the range of 95–97%, which is favorable for pure oxygen production.

4.2. Oxygen permeation: experimental

Fig. 5 shows temperature and membrane thickness dependence of oxygen permeation flux through the BSCF

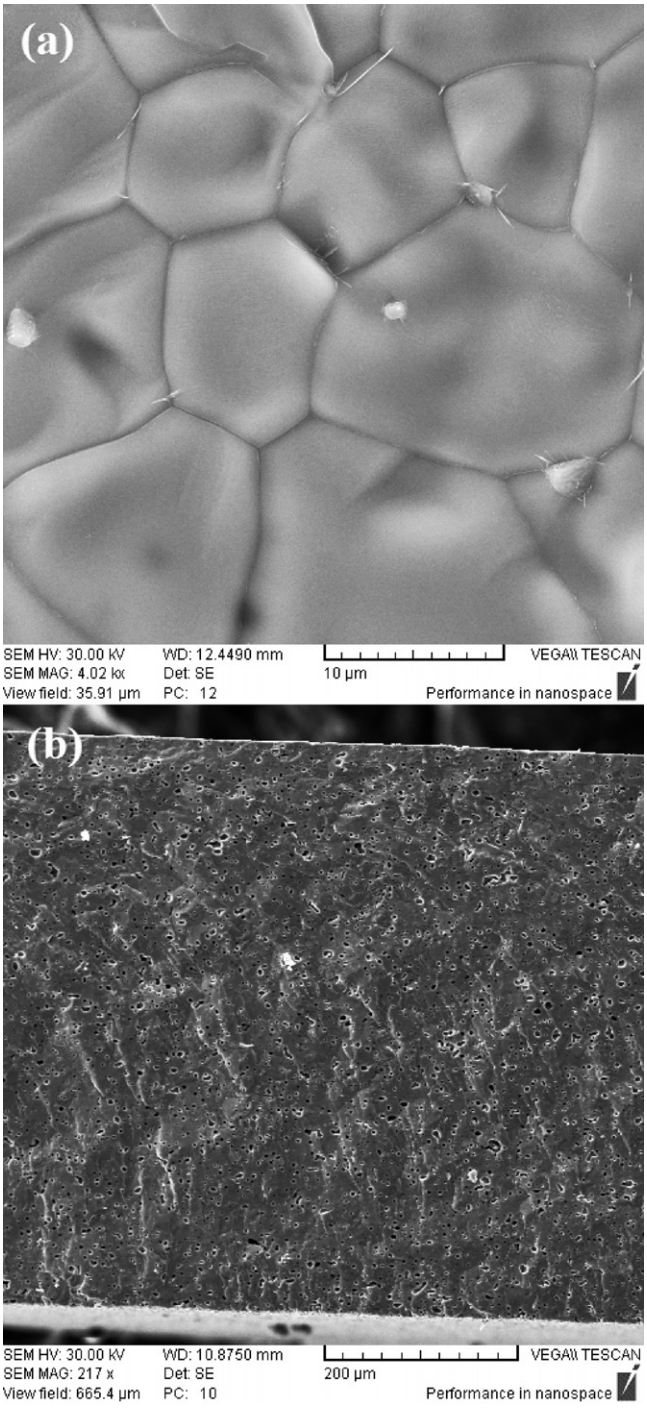

Fig. 4. SEM micrograph of surface (a) and cross section (b) of the BSCF membrane, pressed under 400 MPa, sintered at 1100 °C for 10 h.

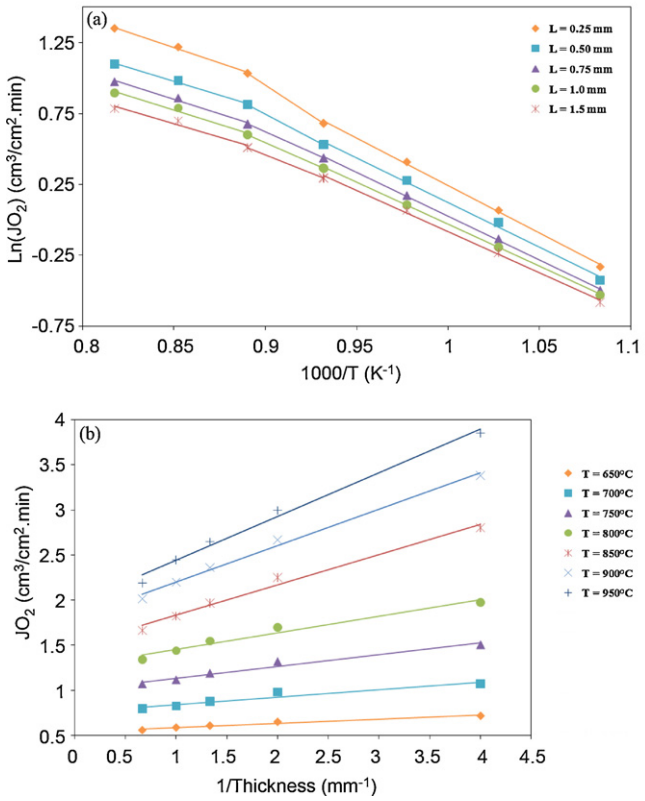

Fig. 5. (a) Temperature and (b) membrane thickness dependence of oxygen permeation flux through the BSCF membranes; q_{feed} = 150 cm^3/min, $q_{sweep\text{-}gas}$ = 60 cm^3/min.

membranes. According to Fig. 5a, there are two ranges for activation energy of oxygen permeation. The critical temperature for activation energy change is around 825 °C. The following equation was used for predicting effect of temperature on experimental oxygen permeation flux.

$$J_{O_2} = k_{app}\exp\left(-\frac{E_{app}}{\bar{R}T}\right) \quad (20)$$

Linear least square (LLS) method was used for obtaining constants of this equation. Calculated activation energy of oxygen permeation values are summarized in Table 3. As can be seen, activation energy of oxygen permeation at low temperature (650–800 °C) is about 50% more than that at high temperature (650–800 °C). As shown, at lower temperatures, effect of temperature is more significant; because at lower temperature, diffusion coefficient and surface reaction rates are very small and increasing temperature results in significant changes in their values; however at higher temperature, their values does not change significantly with temperature. So, activation energy at low temperature is more than that at high temperature. Also, it can be seen that, membrane thickness has a minor effect on activation energy of oxygen permeation. Increasing membrane thickness from 0.25 to 1.50 mm leads to 15% activation energy reduction.

Table 3
Activation energy of oxygen permeation through the BSCF membranes.

Membrane thickness (mm)	Activation energy (kJ/mol)	
	650–800 °C	800–950 °C
0.25	55.60	36.38
0.50	52.36	32.82
0.75	51.11	34.01
1.00	49.16	33.77
1.50	48.22	31.71

For a relatively thick membrane, the diffusion process is commonly the slowest step. The Wagner theory can be used to describe the oxygen permeation flux in this case [24]

$$J_{O_2} = \frac{\bar{R}T}{4^2F^2L}\left(\frac{\sigma_i\sigma_e}{\sigma_i+\sigma_e}\right)\ln\left(\frac{p'_{O_2}}{p''_{O_2}}\right) \quad (21)$$

As can be seen, this theory predicts an inverse linear dependence of oxygen permeation flux to membrane thickness. So, if a membrane obeys this relationship, bulk diffusion is limiting step of oxygen permeation flux through it. Fig. 5b shows oxygen permeation flux through the BSCF membranes versus inverse of membrane thickness. As can be seen, the relation between J_{O_2} and $1/L$ is nearly linear at all temperatures. So, it can be concluded that, bulk diffusion is the limiting step of oxygen permeation flux through the BSCF membranes at the conditions of experiments.

Fig. 6 shows effects of temperature, feed and permeate side oxygen partial pressures, feed and sweep gas flow rates and membrane thickness on oxygen permeation flux through the BSCF membranes. Specific operating conditions of experimental oxygen permeation data which are illustrated in this figure, are summarized in Table 4. It is worthwhile to mention that all parameters calculated and presented in this work were determined at the same conditions of experimental oxygen permeation data as indicated in Table 4.

Temperature has a favorable effect on oxygen permeation due to acceleration of bulk diffusion and surface exchange reactions due to increasing diffusion coefficient and surface reaction rates at elevated temperatures, respectively. Fig. 6a presents influence of feed side oxygen partial pressure on oxygen permeation flux. As can be seen oxygen permeation flux increases with feed side oxygen partial pressure. As oxygen partial pressure increases, the driving force of the whole process increases and thus oxygen permeation flux enhances. This effect is more significant at lower oxygen partial pressure. Fig. 6b shows effect of permeate side oxygen partial pressure on oxygen permeation. By increasing oxygen partial pressure at permeate side, permeation driving force decreases and thus oxygen permeation flux decreases. Fig. 6c indicates effect of feed flow rate on oxygen permeation flux. Increasing feed flow rate, up to 100–150 cm^3/min, enhances oxygen permeation flux, but beyond that it slightly affects oxygen permeation flux. Fig. 6d presents effect of sweep gas flow rate on oxygen permeation flux. Increasing sweep gas flow rate leads to increasing oxygen permeation flux. This is due to

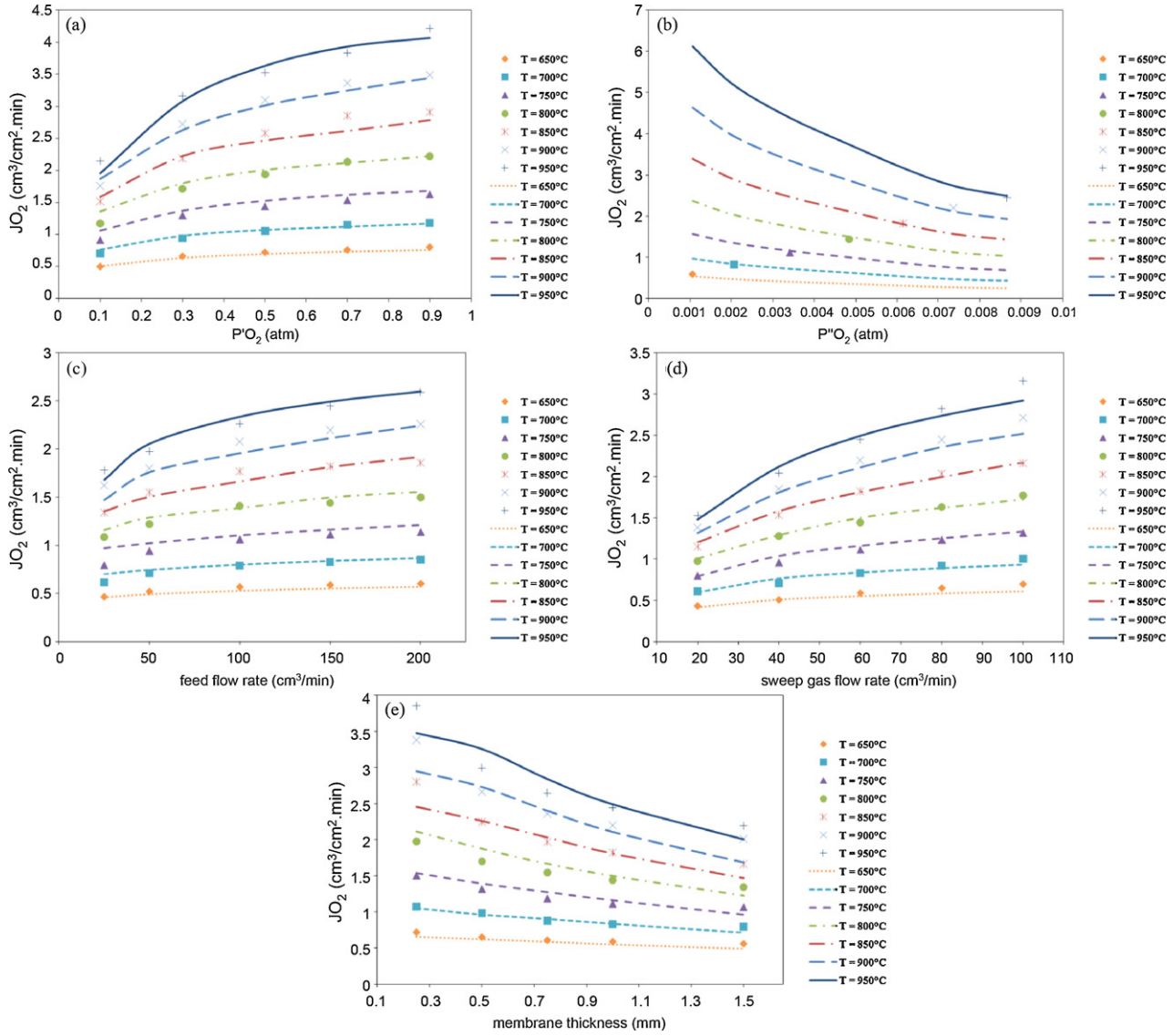

Fig. 6. Effects of (a) feed side oxygen partial pressure, (b) permeate side oxygen partial pressure, (c) feed flow rate, (d) sweep gas flow rate and (e) membrane thickness, on oxygen permeation flux. Points are experimental data and lines are model prediction. Operating conditions are summarized in Table 4.

decreasing oxygen partial pressure in permeate side and increasing partial pressure difference across the membrane, which is the driving force of oxygen permeation. Fig. 6e shows effect of membrane thickness on oxygen permeation flux. As shown, increasing membrane thickness leads to lower oxygen permeation flux, because bulk diffusion resistance increases.

4.3. Model validation

To fit the developed model parameters, a nonlinear regression method was used. Root mean square deviation (RMSD) was the objective function for error minimization. Furthermore, to illustrate the accuracy of the developed model, average absolute deviation (AAD) and square of the Pearson

Table 4
Operating conditions for data of Figs. 6, 8 and 9.

Figure part	T (°C)	p'_{O_2} (atm)	$p''_{O_2} \times 10^{-2}$ (atm)	q_{feed} (cm^3/min)	$q_{sweep\ gas}$ (cm^3/min)	L (mm)
a	650–950	0.1–0.9	0.653–5.23	300	60	1
b	650–950	0.21	0.765–3.10	150	60	1
c	650–950	0.21	0.605–3.28	25–200	60	1
d	650–950	0.21	0.545–5.65	150	20–100	1
e	650–950	0.21	0.727–4.80	150	60	0.25–1.5

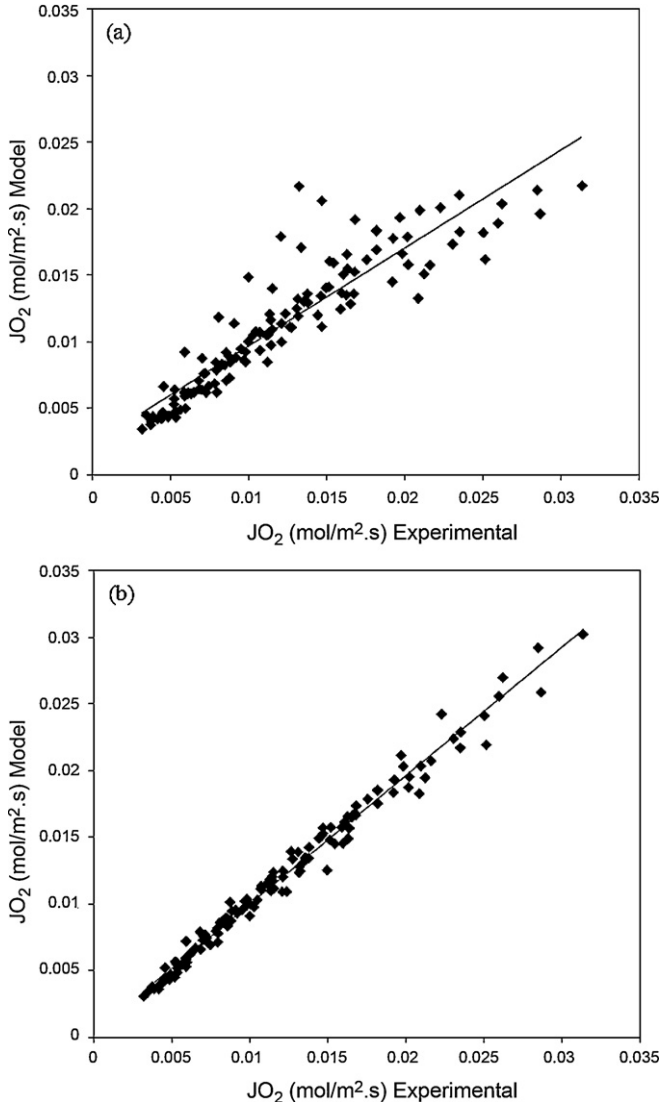

Fig. 7. Comparison between accuracy of (a) the primary and (b) the modified models.

product moment correlation coefficient (R^2) were calculated. Firstly, Eq. (5) was used for estimation of oxygen permeation flux through the BSCF membranes, and the results showed significant errors. As the three correction terms were included in the model, the accuracy of oxygen permeation flux prediction extremely enhanced. When Eq. (5), was used to predict oxygen permeation flux, enormous error was calculated (RMSD = 0.1746, AAD = 0.1218 and R^2 = 0.839), however when the crucial correction terms were added to the model, its accuracy improved significantly (RMSD = 0.0617, AAD = 0.0487 and R^2 = 0.985). Fig. 7 illustrates accuracy of the primary and the modified models by comparing the predicted oxygen permeation fluxes with the experimental data. Table 5 reveals the calculated statistical parameters used as criteria of the model accuracy. Clearly, error is small and the model is able to correlate the experimental data satisfactorily.

4.4. Model constants

As mentioned before, temperature dependence of oxygen vacancy diffusion coefficient and both forward and reverse reaction rate constants were considered to be the Arrhenius type functions. Values of activation energies and pre-exponential coefficients and also constants of the correction terms are summarized in Table 6.

4.5. Oxygen permeation: modeling

Figs. 6 and 8 reveal effects of temperature, feed and permeate side oxygen partial pressures, feed and sweep gas flow rates and membrane thickness on oxygen permeation flux predicted by the model and calculated permeation resistances, respectively. Predicted oxygen permeation flux and permeation resistance were calculated at operating conditions as summarized in Table 4. Effects of these variables on oxygen permeation flux are discussed based on the experimental results and the mathematical modeling predictions.

4.5.1. Effect of temperature

Fig. 6 illustrates effects of temperature on oxygen permeation flux. Enhancement of oxygen permeation flux is clearly observed by increasing temperature. As mentioned before, increasing diffusion coefficient and conductivity of oxygen vacancy improves oxygen permeability. As temperature increases, k_f and k_r increase and since the activation energy of the former is greater than that of the later; k_f is more sensitive to temperature. The forward reaction implies oxygen adsorption on the both membrane surfaces, while the reverse reaction introduces oxygen desorption. As the oxygen transport direction is from the feed side to the permeate side, the

Table 5
Statistical parameters used for model validation.

Statistical parameter	Abbreviation	Formula	Value
Root mean square deviation	RMSD	$\sqrt{\frac{1}{N}\sum_i^N \left(1-\frac{J_{O_2,i}^{calc}}{J_{O_2,i}^{exp}}\right)^2}$	0.0617
Average absolute deviation	AAD	$\frac{1}{N}\sum_i^N \left\lvert 1-\frac{J_{O_2,i}^{calc}}{J_{O_2,i}^{exp}}\right\rvert$	0.0487
Square of the Pearson product moment correlation coefficient	R^2	$\left[\frac{\sum_i^N (J_{O_2,i}^{exp}-J_{O_2}^{exp,ave})(J_{O_2,i}^{calc}-J_{O_2}^{calc,ave})}{\sqrt{\sum_i^N (J_{O_2,i}^{exp}-J_{O_2}^{exp,ave})^2 \sum_i^N (J_{O_2,i}^{calc}-J_{O_2}^{calc,ave})^2}}\right]^2$	0.985

Table 6
Model parameters.

Parameter	Value	Dimension
D_V^0	5.9807×10^{-5}	m^2/s
k_f^0	$4.1688 \times 10^{+1}$	$m/atm^n\ s$
k_r^0	$1.1660 \times 10^{+4}$	$mol/m^2\ s$
E_D	$9.2709 \times 10^{+4}$	J/mol
E_f	$1.4668 \times 10^{+5}$	J/mol
E_r	$1.0291 \times 10^{+5}$	J/mol
n	0.2500	–
a'	0.1015	–
b'	1.8687	–
c'	0.4525	–
a''	0.1891	–
b''	9.3439	–
c''	0.1320	–

forward rate of reaction (r_f) is dominant comparing with the reverse rate of reaction (r_r) at the feed side, but in the permeate side, the reverse rate of reaction is dominant. In each side of the membrane, r_f is functions of temperature, $p^*_{O_2}$ and C_V in that side. As temperature increases, both k_f and C_V increase and thus r_f increases with temperature. However, r_r is an ascending function of only temperature. Both r_f and r_r increase with temperature. In the feed side, r_f is greater than r_r and more sensitive to temperature, while at the permeate side, r_r is greater. Thus, by increasing temperature, the difference between r_f and r_r increases and consequently oxygen permeation flux enhances.

Resistance of surface reaction on each side of the membrane is affected by variation of both k_f and $p^*_{O_2}$ in that side with temperature. As mentioned, D_V and k_f increase with temperature, resulting in reduction of all resistances. This is illustrated

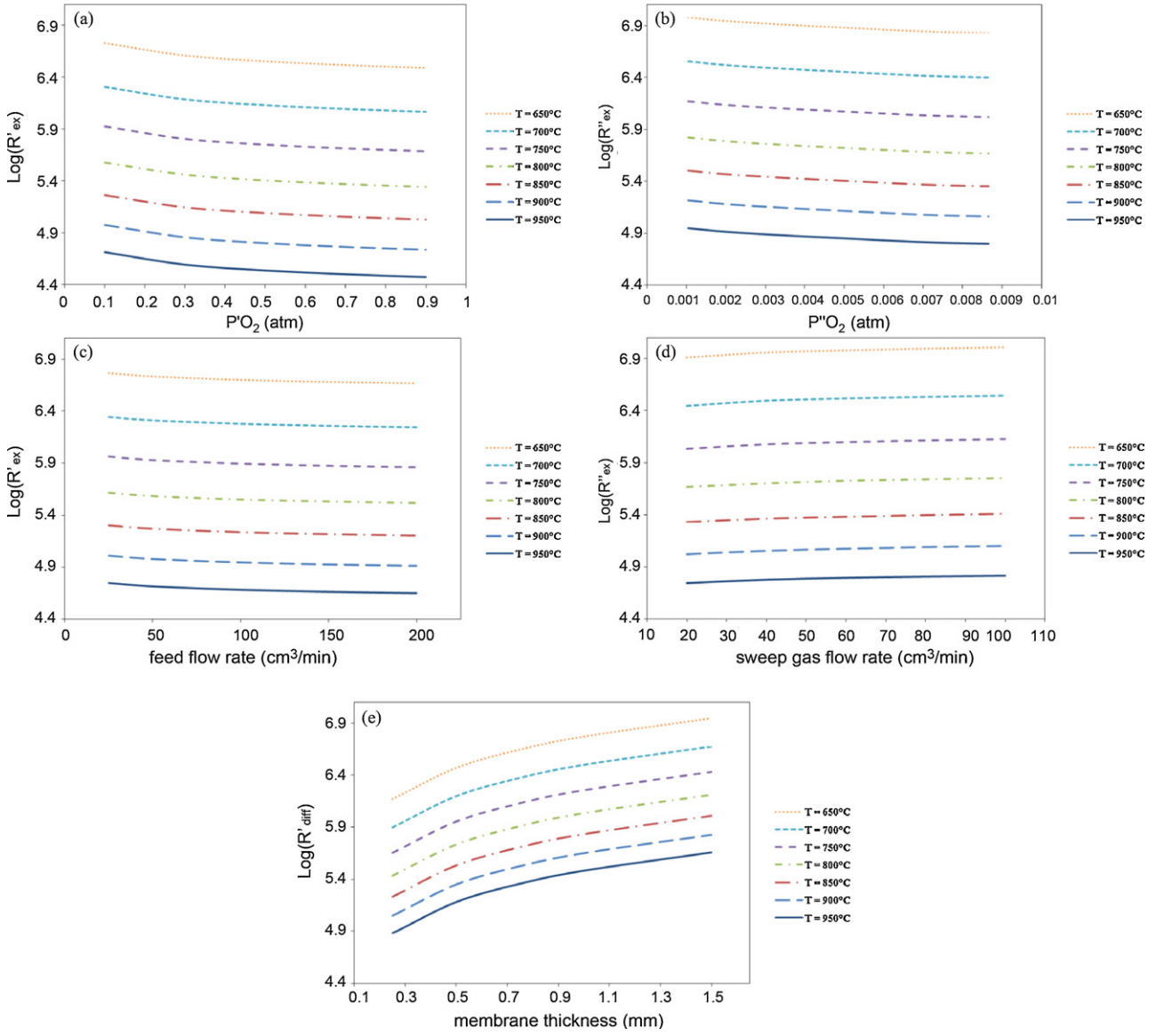

Fig. 8. Effects of (a) feed side oxygen partial pressure, (b) permeate side oxygen partial pressure, (c) feed flow rate, (d) sweep gas flow rate and (e) membrane thickness, on permeation resistances (S/m). Operating conditions are summarized in Table 4.

in Fig. 8. However, as activation energy of diffusion is about one order of magnitude smaller than that of forward surface reaction, resistance of surface reaction decreases more rapidly compared with that of bulk diffusion. At lower temperature (e.g. 650 °C), D_V and k_f are small and grow rapidly with temperature. Consequently, at lower temperature, the resistances change more significantly. As calculations revealed, average contribution of bulk diffusion resistance in total resistance increases from 29.2% to 73.7% as temperature increases from 650 to 950 °C. So, as temperature increases, the contribution of diffusion resistance in total resistance becomes dominant and thus oxygen permeation tends to be limited by diffusion.

$p'^{*}_{O_2}$ depends on temperature only in terms of Re. As temperature increases, viscosity increases, so Re decreases. As mentioned above, the correction term increases with Re and thus $p'^{*}_{O_2}$ decreases with temperature. To sum up, temperature has two different effects on R'_{ex} but as its effect on k_f is more dominant, R'_{ex} decreases with temperature. Temperature dependency of Re and p''_{O_2} result in variation of $p''^{*}_{O_2}$ with temperature. As mentioned, increasing temperature decreases Re and thus the permeate side correction term decreases. At elevated temperatures, oxygen permeation flux increases and this results in higher $p''^{*}_{O_2}$. Since effect of oxygen partial pressure is more dominant, $p''^{*}_{O_2}$ increases with temperature. Both k_f and $p''^{*}_{O_2}$ increase with temperature and consequently as temperature increases, R''_{ex} decreases.

4.5.2. Effect of feed side oxygen partial pressure

Effects of the feed side oxygen partial pressure on oxygen permeation flux are shown in Fig. 6a. As expected, increasing p'_{O_2} enhances the feed side surface reaction rate and increases the permeation driving force. However, this increment is nonlinear. In other words, as the feed side oxygen partial pressure is doubled, the probability of oxygen molecules adsorption into the membrane surface and thus the surface reaction rate promotes less than twice. This is due to the limited number of active reaction sites which is inherently constant. As a result, oxygen permeation flux increases less than twice. Fig. 6a reveals that by doubling p'_{O_2}, J_{O_2} increases about 20%.

As Fig. 8a reveals, by increasing p'_{O_2}, R'_{ex} reduces, while R_{diff} is not affected. In addition, reduction of R'_{ex} and consequently increment of J_{O_2} result in higher p''_{O_2}, thus R''_{ex} decreases very slightly. Contribution of R'_{ex} to the total resistance decreases as temperature increases, while that of R_{diff} increases. Contribution of R''_{ex} to the total resistance increases with increasing the oxygen partial pressure at low temperature, but decreases at high temperature.

4.5.3. Effect of permeate side oxygen partial pressure

Effects of the permeate side oxygen partial pressure on oxygen permeation flux are shown in Fig. 6b. As observed, oxygen permeation flux decreases as the oxygen partial pressure at the permeate side of the membrane increases. This phenomenon is due to the reduction of oxygen permeation driving force. Also, by increasing p''_{O_2} the rate of forward reaction at the permeate side increases, while the rate of reverse reaction remains constant. Consequently, the increment of p''_{O_2} diminishes oxygen permeation flux.

It is clear that p''_{O_2} affects neither R'_{ex} nor R_{diff}. However, as shown in Fig. 8b, R''_{ex} decreases as p''_{O_2} increases. The ratio of R''_{ex}/R'_{ex} is equal to the ratio of $(p'^{*}_{O_2}/p''^{*}_{O_2})^n$. Since $p'^{*}_{O_2}$ is larger than $p''^{*}_{O_2}$, R''_{ex} is greater than R'_{ex}. The results confirm this statement and reveal that R''_{ex} is 1.35–1.98 times larger than R'_{ex}. The calculations showed that, $p''^{*}_{O_2}$ affects the ratio of the permeate side surface reaction resistance over the total resistance, reversely, while those of the bulk diffusion and the feed side surface reaction increase with $p''^{*}_{O_2}$.

4.5.4. Effect of feed flow rate

Effects of the feed flow rate on oxygen permeation flux are presented in Fig. 6c. It is clear that oxygen permeation flux significantly enhances with increasing feed flow rate. However, with increasing feed flow rate beyond 100–150 cm^3/min, oxygen permeation flux increases slightly. The feed side approaches to the well-mixed condition as feed flow rate increases due to the gas phase turbulence increment. Since the well-mixed condition is established asymptotically, the flux improvement rate decreases as flow rate increases. Hydrodynamics of feed flow rate does not significantly affect oxygen permeation flux and thus its effects are reasonably negligible.

Re increases with increasing feed flow rate and consequently, $p'^{*}_{O_2}$ increases and this results in the reduction of R'_{ex}, as shown in Fig. 8c. R_{diff} does not vary with feed flow rate and R''_{ex} decreases as feed flow rate increases. This reduction in R''_{ex} is an indirect effect and is due to the increasing p''_{O_2} because of the oxygen permeation flux improvement. Contribution of R'_{ex} in total resistance decreases with increasing feed flow rate, while contribution of R_{diff} increases. At low temperature, contribution of R''_{ex} in the total resistance increases with increasing feed flow rate, while decreases at high temperature.

4.5.5. Effect of sweep gas flow rate

Fig. 6d represents effects of the sweep gas flow rate on oxygen permeation flux. Greater sweep gas flow rate results in the $p''^{*}_{O_2}$ reduction and this increases oxygen permeation driving force. Consequently, increasing sweep gas flow rate leads to the oxygen permeation flux enhancement.

Equations in Table 2 reveal that only R''_{ex} is affected by sweep gas flow rate. As the sweep gas flow rate increases, two reverse phenomena arise. The first is increasing Re which increases the correction term and the second is reduction of p''_{O_2}, which reduces $p''^{*}_{O_2}$. Since the second phenomenon is dominant, $p''^{*}_{O_2}$ decreases, while sweep gas flow rate increases. Consequently as shown in Fig. 8d, R''_{ex} and thus the total resistance of the oxygen transfer through the membrane increase with increasing the sweep gas flow rate. Besides, oxygen permeation driving force increases and because its effect on oxygen permeation flux is dominant compared with R''_{ex}, oxygen permeation flux enhances, as mentioned before. The contribution of R''_{ex} in the total resistance increases, while the contributions of R'_{ex} and R_{diff} decrease with increasing the sweep gas flow rate.

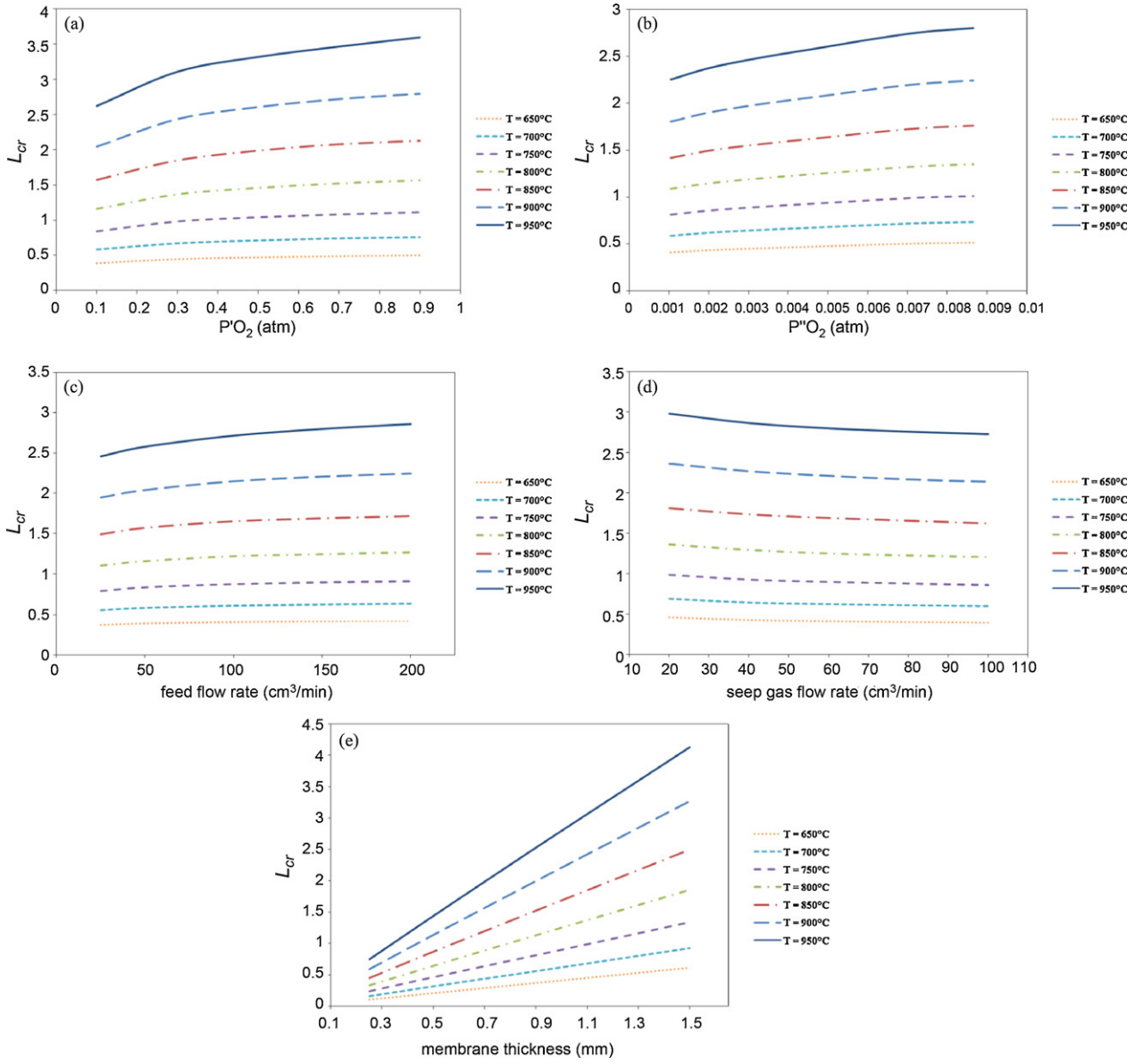

Fig. 9. Effects of (a) feed side oxygen partial pressure, (b) permeate side oxygen partial pressure, (c) feed flow rate, (d) sweep gas flow rate and (e) membrane thickness, on dimensionless characteristic thickness. Operating conditions are summarized in Table 4.

4.5.6. Effect of membrane thickness

Effects of the membrane thickness on oxygen permeation flux are revealed in Fig. 6e. As seen in Fig. 8e, by increasing the membrane thickness, the bulk diffusion resistance increases, and thus, oxygen permeation flux decreases. As R_{diff} increases, p''_{O_2} reduces and consequently R''_{ex} increases. R'_{ex} is not affected by the membrane thickness. The ratio of R_{diff} to the total resistance reduces as the membrane thickness decreases. Thus, as the membrane becomes thinner, the oxygen diffusion limiting features diminish. Meanwhile, contributions of the other two oxygen exchange resistances in the total resistance increase. This behavior continues till the membrane thickness approaches a specific value which is the membrane characteristic thickness. At the membrane characteristic thickness, the surface exchange reactions and the bulk diffusion contribute equally each other to limit oxygen permeation flux. For membranes which are thinner than their characteristic thickness, the bulk diffusion is not further the rate-limiting step for the permeation.

4.6. Dimensionless characteristic thickness

Fig. 9 shows effects of temperature, oxygen partial pressures and flow rates on the membrane dimensionless characteristic thickness. Operating conditions for calculation of dimensionless characteristic thickness are summarized in Table 4. Clearly, L_{cr} increases with temperature, but at elevated temperature, increases more rapidly than at low temperature. The surface exchange reactions and also the bulk diffusion resistances decrease as temperature increases. As mentioned before, the surface reactions resistances are stronger functions of temperature compared with the bulk diffusion resistance.

Thus, R'_{ex} and R''_{ex} decrease more rapidly compared with R_{diff}. Consequently, as temperature increases L_{cr} tends to become greater and this means that oxygen permeation flux trough the membrane tends to be limited by the bulk diffusion. The results revealed that approximately in half of the experiments, the bulk diffusion resistance was the permeation rate-limiting step. Average value of L_{cr} was calculated to be 1.380, indicating that the main oxygen permeation resistance is the bulk diffusion, and oxygen permeation flux is improved by decreasing the membrane thickness.

As mentioned before, by increasing the feed side oxygen partial pressure, both R'_{ex} and R''_{ex} decrease, while R_{diff} does not vary. This results in increasing L_{cr} as p'_{O_2} increases. The functionality of L_{cr} with p''_{O_2} is almost the same as p'_{O_2}. However, p''_{O_2} only affects R''_{ex} and not R'_{ex}. As stated previously, R''_{ex} decreases, and thus, L_{cr} increases with p''_{O_2}. To sum up, these behaviors illustrate that by increasing the feed and permeate side oxygen partial pressures, oxygen permeation flux is limited by the bulk diffusion. As mentioned previously, the feed flow rate increment results in the reduction of R'_{ex} and R''_{ex}, while R_{diff} remains constant. Thus, L_{cr} increases with the feed flow rate. However, R''_{ex} increases with the sweep gas flow rate, while R'_{ex} and R_{diff} does not vary. Thus, increasing sweep gas flow rate influences L_{cr} reversely. R_{diff} is a direct linear function of membrane thickness (L) and R'_{ex} is independent of L. R''_{ex} increases very slightly with L because R''_{ex} is reverse function of $p''^{*}_{O_2}$ which decreases with L. So, change in $R'_{ex} + R''_{ex}$ with membrane thickness is negligible and hence L_{cr} increases linearly with the membrane thickness.

5. Conclusion

The $Ba_{0.5}Sr_{0.5}Co_{0.8}Fe_{0.2}O_{3-\delta}$ membranes were synthesized using EDTA/citrate complexation method and effects of operating conditions on oxygen permeation flux were investigated. A mathematical model was developed to study oxygen permeation flux through the BSCF membranes. The distinctive features of the developed model can be summarized as follows:

- the model can predict oxygen permeation flux extremely accurate (RMSD = 0.0617, AAD = 0.0487 and $R^2 = 0.985$);
- the model is an explicit function of all operating parameters;
- the both bulk diffusion and surface exchange kinetics are incorporated into the model;
- the forward and reverse surface reactions are assumed non elementary;
- the feed and sweep gas flow rates are incorporated into the model via definition of the modified oxygen partial pressure;
- the effects of system hydrodynamics, flow rates and properties of entering fluids are taken into account with the aid of a Reynolds number in the modified oxygen partial pressure definition;
- the model is capable to calculate oxygen vacancy bulk diffusion coefficient, forward and reverse surface exchange rate constants and permeation resistances;
- membrane dimensionless characteristic thickness is defined and calculated as a criterion for determining the limiting permeation step.

The results illustrated that by increasing temperature, permeation flux improves. This is due to increasing oxygen vacancy diffusion coefficient and conductivity and forward and reverse reaction rate constants. Also, by increasing the feed side oxygen partial pressure, oxygen permeation driving force and the feed side surface reaction rate increase, and this results in higher oxygen permeation flux. However, by increasing the permeate side oxygen partial pressure, the driving force decreases and hence oxygen permeation flux decreases. Increasing the feed and sweep gas flow rates results in the higher driving force and thus significantly enhances oxygen permeation flux, but beyond feed flow rate of 100–150 cm^3/min, oxygen permeation flux does not increase significantly. By increasing the membrane thickness, the bulk diffusion resistance increases and oxygen permeation flux decreases.

As temperature increases, the forward reaction rate constant and the oxygen vacancy diffusion coefficient increase, so all the three resistances decrease. Increasing the feed side oxygen partial pressure, directly affects the feed side surface reactions resistance and reduces it, however, indirectly influences and reduces the permeate side surface reactions resistance. Increasing the permeate side oxygen partial pressure reduces the permeate side surface reactions resistance. The greater feed flow rate results in reduction of the feed side surface reactions resistance. However, the permeate side surface reactions resistance is affected indirectly and decreases with the feed flow rate. The permeate side surface reactions resistance increases with the sweep gas flow rate. The thicker membrane results in the higher bulk diffusion resistance.

The dimensionless characteristic thickness of membrane increases with temperature and thus oxygen permeation flux through the membrane tends to be limited by bulk diffusion at temperature higher than 750–800 °C. The dimensionless characteristic thickness increases with increasing the oxygen partial pressures and feed flow rate, however it decreases with the sweep gas flow rate. The dimensionless characteristic thickness varies from 0.11 up to 4.13 and this illustrates that contribution of the bulk diffusion resistance to the total resistance is in the range of 9.6–81%. Thus, the developed model based on the experimental data is valid for the both bulk diffusion and surface exchange kinetics-limiting cases.

Notation

a, b, c, n	constant of correction terms
C	molar concentration
D	diffusion coefficient
E	activation energy
F	Faraday constant
J	molar flux density
k	surface exchange rate constant
L	thickness
p_{O_2}	oxygen partial pressure

q	volumetric flow rate
$\bar{R}$	universal gas constant
R	resistance
r	rate of reaction
t_i	transference number
T	temperature
u	fluid velocity
z_i	valence

Greek letters

λ	distance between the air entrance and membrane surface
$\tilde{\mu}$	electrochemical potential
ν	kinematic viscosity
ρ	density
σ	conductivity
ϕ	electric potential

Subscripts and superscripts

app	apparent
c	characteristic
cr	characteristic, dimensionless
diff	diffusion
e	electronic
ex	surface exchange reaction
f	forward reaction
g	gas phase
h	electron hole
i	ionic
O	oxygen ion or atom
O_2	oxygen molecule
r	reverse reaction
s	surface phase
V	vacancy
$'$	feed side
$''$	permeate side
$\times$	zero charge
$\bullet$	single positive charge

References

[1] B. Suresh, S. Schlag, K. Yokose, Y. Ping, Air separation gases, in: The Chemical Economics Handbook Marketing Research Report, 2008.

[2] A. Pavone, Options for procuring oxygen, in: Process Economics Program Review, 1991.

[3] Y. Liu, X. Tan, K. Li, Mixed conducting ceramics for catalytic membrane processing, Catalysis Reviews: Science and Engineering 48 (2006) 145–198.

[4] W. Zhou, R. Ran, Z. Shao, Progress in understanding and development of $Ba_{0.5}Sr_{0.5}Co_{0.8}Fe_{0.2}O_{3-\delta}$ based cathodes for intermediate-temperature solid-oxide fuel cells: a review, Journal of Power Sources 192 (2009) 231–246.

[5] Y. Teraoka, H.M. Zhang, S. Furukawa, N. Yamazoe, Oxygen permeation through perovskite-type oxides, Chemistry Letters 14 (1985) 1743–1746.

[6] Y. Teraoka, T. Nobunaga, N. Yamazoe, Effect of cation substitution on the oxygen semipermeability of perovskite-type oxides, Chemistry Letters 17 (1988) 503–506.

[7] Y. Teraoka, H.M. Zhang, K. Okamoto, N. Yamazoe, Mixed ionic-electronic conductivity of $La_{1-x}Sr_xCo_{1-y}Fe_yO_{3-\delta}$ perovskite-type oxides, Materials Research Bulletin 23 (1988) 51–58.

[8] Z. Shao, W. Yang, Y. Cong, H. Dong, J. Tong, G. Xiong, Investigation of the permeation behavior and stability of a $Ba_{0.5}Sr_{0.5}Co_{0.8}Fe_{0.2}O_{3-\delta}$ oxygen membrane, Journal of Membrane Science 172 (2000) 177–188.

[9] A. Leo, S. Smart, S. Liu, J.C. Diniz da Costa, High performance perovskite hollow fibres for oxygen separation, Journal of Membrane Science 368 (2011) 64–68.

[10] A. Kovalevsky, C. Buysse, F. Snijkers, A. Buekenhoudt, J. Luyten, J. Kretzschmar, S. Lenaerts, Oxygen exchange-limited transport and surface activation of $Ba_{0.5}Sr_{0.5}Co_{0.8}Fe_{0.2}O_{3-\delta}$ capillary membranes, Journal of Membrane Science 368 (2011) 223–232.

[11] Q. Jiang, K.J. Nordheden, S.M. Stagg-Williams, Oxygen permeation study and improvement of $Ba_{0.5}Sr_{0.5}Co_{0.8}Fe_{0.2}O_x$ perovskite ceramic membranes, Journal of Membrane Science 369 (2011) 174–181.

[12] C. Wessel, M.W. Lumey, R. Dronskowski, First-principles electronic-structure calculations on the stability and oxygen conductivity in $Ba_{0.5}Sr_{0.5}Co_{0.8}Fe_{0.2}O_{3-\delta}$, Journal of Membrane Science 366 (2011) 92–96.

[13] S. Engelsa, T. Markusb, M. Modigella, L. Singheiser, Oxygen permeation and stability investigations on MIEC membrane materials under operating conditions for power plant processes, Journal of Membrane Science 370 (2011) 58–69.

[14] B. Rutkowski, J. Malzbender, T. Beck, R.W. Steinbrech, L. Singheiser, Creep behaviour of tubular $Ba_{0.5}Sr_{0.5}Co_{0.8}Fe_{0.2}O_{3-\delta}$ gas separation membranes, Journal of the European Ceramic Society 31 (2011) 493–499.

[15] A. Chanda, B.X. Huang, J. Malzbender, R.W. Steinbrech, Micro- and macro-indentation behaviour of $Ba_{0.5}Sr_{0.5}Co_{0.8}Fe_{0.2}O_{3-d}$ perovskite, Journal of the European Ceramic Society 31 (2011) 401–408.

[16] K. Efimov, T. Halfer, A. Kuhn, P. Heitjans, J. Caro, A. Feldhoff, Novel cobalt-free oxygen-permeable perovskite-type membrane, Chemistry of Materials 22 (2010) 1540–1544.

[17] S. Kim, Y.L. Yang, A.J. Jacobson, B. Abeles, Diffusion and surface exchange coefficients in mixed ionic electronic conducting oxides from the pressure dependence of oxygen permeation, Solid State Ionics 106 (1998) 189–195.

[18] S. Li, W. Jin, N. Xu, J. Shi, Synthesis and oxygen permeation properties of $La_{0.2}Sr_{0.8}Co_{0.2}Fe_{0.8}O_{3-\delta}$ membranes, Solid State Ionics 124 (1999) 161–170.

[19] S.J. Xu, W.J. Thomson, Oxygen permeation rates through ion-conducting perovskite membranes, Chemical Engineering Science 54 (1999) 3839–3850.

[20] Z. Yang, Y.S. Lin, A semi-empirical equation for oxygen nonstoichiometry of perovskite-type ceramics, Solid State Ionics 150 (2002) 245–254.

[21] X. Tan, K. Li, Modeling of air separation in a LSCF hollow-fiber membrane module, AIChE Journal 48 (2002) 1469–1477.

[22] X. Tan, Y. Liu, K. Li, Mixed conducting ceramic hollow-fiber membranes for air separation, AIChE Journal 51 (2005) 1991–2000.

[23] X. Tan, K. Li, Oxygen production using dense ceramic hollow fiber membrane modules with different operating modes, AIChE Journal 53 (2007) 838–845.

[24] J. Sunarso, S. Baumann, J.M. Serra, W.A. Meulenberg, S. Liu, Y.S. Lin, J.C. Diniz da Costa, Mixed ionic–electronic conducting (MIEC) ceramic-based membranes for oxygen separation, Journal of Membrane Science 320 (2008) 13–41.

[25] S. Engels, F. Beggel, M. Modigell, H. Stadler, Simulation of a membrane unit for oxyfuel power plants under consideration of realistic BSCF membrane properties, Journal of Membrane Science 359 (2010) 93–101.

[26] K. Kontturi, L. Murtomäki, J.A. Manzanares, Ionic Transport Processes: In Electrochemistry and Membrane Science, Oxford University Press Inc., New York, 2008.

[27] K.S. Goto, Solid State Electrochemistry and Its Applications to Sensors and Electronic Devices, Elsevier, Amsterdam, 1998.

[28] A. Ghadimi, M.A. Alaee, A. Behrouzifar, A.A. Asadi, T. Mohammadi, Oxygen permeation of $Ba_xSr_{1-x}Co_{0.8}Fe_{0.2}O_{3-\delta}$ perovskite-type

membrane: experimental and modeling, Desalination 270 (2011) 64–75.

[29] Z. Shao, G. Xiong, H. Dong, W. Yang, L. Lin, Synthesis, oxygen permeation study and membrane performance of a $Ba_{0.5}Sr_{0.5}Co_{0.8}Fe_{0.2}O_{3-\delta}$ oxygen-permeable dense ceramic reactor for partial oxidation of methane to syngas, Separation and Purification Technology 25 (2001) 97–116.

[30] H.J.M. Bouwmeester, A.J. Burggraaf, Dense ceramic membranes for oxygen separation, in: A.J. Burggraaf, L. Cot (Eds.), Fundamentals of Inorganic Membrane Science and Technology, Elsevier Science B.V., Amsterdam, 1996.

[31] H. Koster, F.H.B. Mertins, Powder diffraction of the cubic perovskite $Ba_{0.5}Sr_{0.5}Co_{0.8}Fe_{0.2}O_{3-\delta}$, Powder Diffraction 18 (2003) 56–59.